A Historically Validated Thermal-Hydraulic MOOSE Model of the XE-Prime Nuclear Thermal Rocket Engine: Part I - Model Development and Design Prediction Benchmark

Research Paper

Robert Demuth[1], Andrew Hanson[1], Ruixian Fang[1], Jason Reynolds[2], Travis Knight[1]

Affiliations

University of South Carolina: University of South Carolina, Department of Mechanical Engineering, 300 Main Street, Columbia, SC 29201, USA
NASA Marshall Space Flight Center: NASA Marshall Space Flight Center, Huntsville, AL 35812, USA

Corresponding author

Travis Knight, University of South Carolina; knighttw@cec.sc.edu

Acknowledgements

This work is a collaboration between the University of South Carolina and NASA Marshall Space Flight Center. This research made use of Idaho National Laboratory's High Performance Computing systems located at the Collaborative Computing Center and supported by the Office of Nuclear Energy of the U.S. Department of Energy and the Nuclear Science User Facilities under Contract No. DE-AC07-05ID14517, as well as the University of South Carolina Research Computing Hyperion High Performance Computing cluster, located in the University of South Carolina data center and supported by the Division of Information Technology Research Computing program. The authors thank Jonathan Witter (BWX Technologies, Inc.) for providing an extensive collection of historical Rover/NERVA documentation and reports that supported this work. The authors also thank Andrew Ghossein (Lockheed Martin) for providing additional XE-Prime documentation and historical references. The authors acknowledge the contribution of the 2025 Cosmic intern team at Idaho National Laboratory (Jonathan Geymer, Leo Tunkle, Wafaa Osman, and Felicity Griffin) for providing example inputs for automated OpenMC cross-section tabulation workflows used in the development of the Python scripting tools utilized in this work. The authors additionally acknowledge Jackson Harter (Idaho National Laboratory) for his continued guidance, technical mentorship, and expertise in MOOSE-based NTP modeling and autonomous reactor control methodologies, which contributed significantly to the development of this work.

Preprint not peer reviewed

This preprint research paper has not been peer reviewed. Electronic copy available at: https://ssrn.com/abstract=7593512

A Historically Validated Thermal-Hydraulic MOOSE Model of the XE-Prime Nuclear Thermal Rocket Engine: Part I – Model Development and Design Prediction Benchmark

Robert Demuth[a], Andrew Hanson[a], Jason Reynolds[b], Ruixian Fang[a] and Travis Knight[a,*]

[a]University of South Carolina, Department of Mechanical Engineering, 300 Main Street, Columbia, SC, 29201, USA
[b]NASA Marshall Space Flight Center, Huntsville, AL, 35812, USA

ARTICLE INFO

Keywords:
nuclear thermal propulsion (NTP)
XE-Prime
Rover/NERVA
MOOSE
thermal hydraulics
space nuclear power (SNP)
design benchmark

ABSTRACT

A high-fidelity thermal-hydraulic model of the XE-Prime nuclear thermal rocket engine was developed using MOOSE-based thermal-hydraulic and heat-conduction tools. The objective is to establish a historically benchmarked thermal-hydraulic reference model for future nuclear thermal propulsion fuel performance, neutronic feedback, and transient analyses. This Part I paper establishes the model architecture and benchmarks its steady-state internal response against historical design-prediction calculations.

The model represents the core, reflector, and shield using coupled one-dimensional flow channels and two-dimensional heat-conduction models, with detailed three-dimensional heat conduction within a representative fuel cluster. It uses equivalent fuel and tie flow channels, conjugate heat transfer between coolant and solid regions, prescribed power deposition, temperature-dependent solid material properties, and hydrogen thermophysical properties over the reactor operating range.

Design-prediction benchmarking is performed against historical calculations from the XE-1 Nuclear Subsystem Thermal and Nuclear Design Data Book. Predictions agree well with the XE-1 design report for fuel-channel pressure, hydrogen temperature and density, Reynolds number, heat flux, heat transfer coefficient, solid fuel temperature, tie-channel pressure, tie-channel gas temperature, tie wall temperature, and average tie-block temperature. The comparisons show that the model reproduces the dominant axial trends for the shared XE-1, XE-2, and XE-Prime reactor design, with the largest differences near inlet-region flow-development features.

Overall, the model captures the dominant physics governing XE-Prime thermal-hydraulic operation and establishes a historically benchmarked thermal-hydraulic reference model. Experimental validation of the model against steady-state and transient measurements from the XE-Prime EP-5C full-power experiment is presented in the companion Part II study [1].

1. Introduction

1.1. Nuclear Thermal Propulsion Background

Nuclear thermal propulsion (NTP) systems use a nuclear fission reactor to heat a hydrogen propellant, which is then expanded through a nozzle to generate thrust. A schematic of a representative nuclear thermal rocket engine is shown in Figure 1 [2].

Compared to conventional chemical propulsion systems, NTP systems can achieve significantly higher exhaust velocities and specific impulse due to the low molecular weight of hydrogen and the high temperatures attainable within the reactor core. Historical NTP studies report specific impulse values approximately two to three times greater than advanced chemical propulsion systems [3]. The U.S. nuclear rocket program began in 1955 under Rover and progressed into the Nuclear Engine for Rocket Vehicle Application program, or NERVA. Rover established the reactor physics, fuel, materials, and nuclear test basis for hydrogen-cooled graphite reactors, while NERVA advanced the technology toward integrated engine operation. The development path moved from early proof-of-concept reactor experiments toward reactor systems with improved fuel durability, thermal performance, and engine-level control. The KIWI tests demonstrated the feasibility of a high-temperature, hydrogen-cooled nuclear rocket reactor; the NRX series advanced fuel and reactor performance; and NRX/EST demonstrated integrated engine-system behavior, including startup, shutdown, cooldown, restart, and operation over a broad range of conditions [4–6].

The XE-type NERVA reactor represented the final integrated engine configuration of this development sequence. The XE program incorporated the reactor and engine-system lessons developed during the earlier Rover/NERVA campaigns and advanced the technology toward a flight-relevant ground-test engine. XE-Prime demonstrated automatic startup, closed-loop pressure and temperature control, sustained full-power operation, and practical operation within the ETS-1 test facility. The XE-type design therefore provides a mature and well-documented reference configuration for modern thermal-hydraulic model development [4, 6, 7].

*Corresponding author
Email address: knighttw@cec.sc.edu (T. Knight)
ORCID(s): 0000-0002-8243-3138 (R. Demuth); 0009-0000-9876-4807 (A. Hanson); 0000-0002-8443-3967 (J. Reynolds); 0000-0002-1445-8325 (R. Fang); 0000-0002-8517-7395 (T. Knight)

Preprint not peer reviewed

This preprint research paper has not been peer reviewed. Electronic copy available at: https://ssrn.com/abstract=7593512

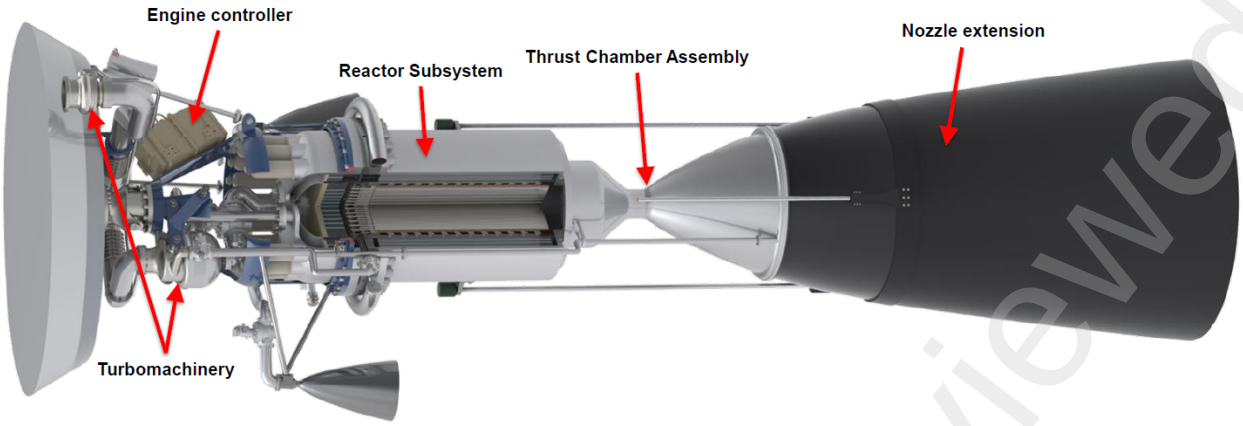

Figure 1: Nuclear Thermal Rocket Engine System. Image sourced from [2].

1.2. XE-1, XE-2, and XE-Prime as a Shared Thermal-Hydraulic Design Basis

The present work treats XE-1, XE-2, and XE-Prime as members of the same XE-type NERVA reactor design family for the purpose of thermal-hydraulic model development and design-prediction benchmarking. The XE-type reactor consisted of a hydrogen-cooled graphite-based core surrounded by a beryllium reflector with rotating control drums, an upper shield and core support plate, a pressure vessel, and a nozzle. Hydrogen flowed through the reflector, shield/support plate, fuel-element coolant channels, tie-element passages, and associated bypass or bleed paths before exiting through the nozzle.

The XE-1 Nuclear Subsystem Thermal and Nuclear Design Data Book provides the primary design basis for the thermal-hydraulic model because it contains the most complete internal reactor design-prediction dataset available for the XE-type configuration [7]. These design calculations include internal quantities that were not directly measurable during engine tests, including fuel-channel pressure, hydrogen temperature, hydrogen density, Reynolds number, heat flux, heat-transfer coefficient, average fuel temperature, tie-channel pressure, tie-channel gas temperature, tie-channel wall temperature, and average tie-block temperature.

1.3. Motivation for Thermal-Hydraulic Design-Prediction Benchmarking

The historical XE-1 design report provides a valuable benchmark because it contains detailed predictions of internal reactor thermal-hydraulic quantities under nominal operating conditions. These data enable comparison of calculated axial fuel-element and tie-element temperature distributions and coolant flow behavior, providing a more rigorous assessment than comparisons based solely on external engine measurements. Demonstrating agreement with these design predictions establishes confidence that the present model accurately reproduces the expected thermal-hydraulic behavior of the XE-type reactor. The benchmarked quantities form the foundation for future multiphysics coupling. Fuel temperature is the dominant solid-temperature feedback parameter governing Doppler reactivity effects, while hydrogen temperature and density determine the moderation characteristics and coolant reactivity feedback within the flow channels. Accurate prediction of these quantities is therefore essential not only for thermal-hydraulic fidelity but also for credible coupled neutronics simulations.

Recent XE-Prime modeling studies provide complementary reference points for modern analysis. Eck and Kotlyar developed a reproducible Serpent benchmark for dry, zero-power XE-Prime conditions, while Thomsen et al. applied coupled Monte Carlo neutronics and thermal-hydraulics to hot-condition XE-Prime analysis using CFD and a reduced-order solver [8, 9]. The present work complements these efforts by focusing on a MOOSE-based reactor-level thermal-hydraulic model benchmarked against the detailed internal XE-1 design-prediction data.

1.4. Objectives

The objective of this work is to develop a high-fidelity MOOSE-based thermal-hydraulic model of the XE-type NERVA reactor and benchmark its internal steady-state response against the XE-1 design-prediction calculations. The model represents the core, reflector, and shield cooling paths using coupled one-dimensional flow channels and reduced-order heat structures, with detailed three-dimensional heat conduction applied within a representative fuel cluster.

This study constitutes Part I of a two-part model development and validation effort. Part I documents the thermal-hydraulic model development and evaluates its implementation against the detailed internal reactor predictions available from the XE-1 design report. The companion Part II study [1] subsequently evaluates the same model against measured steady-state and transient data from the XE-Prime EP-5C full-power experiment. Together, the design-prediction benchmark and experimental validation establish the historical basis for assessing the model across both internal reactor behavior and measured engine operation.

This article documents the model architecture, governing equations, boundary conditions, equivalent-channel treatment, pressure-loss models, material properties, hydrogen property treatment, heat-transfer correlations, and

This preprint research paper has not been peer reviewed. Electronic copy available at: https://ssrn.com/abstract=7593512

prescribed power distributions. The benchmark compares predicted axial fuel-element and tie-element profiles against the XE-1 design report, establishing the thermal-hydraulic reference model subsequently evaluated against experiment in Part II.

2. XE-Prime Thermal-Hydraulic Design Overview

This section summarizes the reactor and engine features needed to interpret the XE-Prime thermal-hydraulic model. For the purposes of this paper, XE-1, XE-2, and XE-Prime are treated as the same NERVA solid-core architecture: a hydrogen-cooled graphite/uranium-carbide core, a beryllium reflector with rotating control drums, an upper shield and support plate, a pressure vessel, and a nozzle. The XE-1 data book is the primary geometry and material reference because it contains the most complete as-built reactor information [7].

2.1. Engine Architecture

XE-Prime used hydrogen as both propellant and reactor coolant. Figure 2 illustrates the hydrogen flow path through the engine. Hydrogen is pumped from the propellant tank, routed through the nozzle, up through the reflector, and down through the shield and core support plate before entering the core, where the majority of the heating occurs. The heated hydrogen is then expanded through the nozzle to generate thrust. A smaller hot-bleed stream is used to drive the turbine-pump system before being exhausted or mixed downstream. This creates a tightly coupled system where reactor power, hydrogen mass flow, turbomachinery behavior, and drum motion all affect the transient response.

For reactor-level modeling, the engine can be reduced to coupled flow paths through the nozzle tubes, reflector, shield/support plate, fuel elements, and tie-rod elements. These channels share the same overall pressure-drop constraint while receiving different nuclear heat loads. The main heat addition occurs in the fuel elements, but reflector, shield, support plate, tie-rod, and nozzle heating are retained because they affect coolant temperature, material temperature, and feedback.

2.2. Core Configuration

The core is comprised of a hexagonal lattice of fuel and tie elements, as illustrated in Figure 3. The full-core representation contains 1,584 fuel elements and 289 tie elements, of which 24 tie elements are shimmed.

The fuel element consists of a graphite matrix containing uranium-carbide fuel particles and nineteen hydrogen coolant channels. The tie element is an unfueled element that contains a central tie rod, stainless steel liner, pyrographite insulating sleeve, and annular hydrogen cooling channel. These two element types are the basis for the representative fuel cluster used in the thermal-hydraulic heat-conduction model.

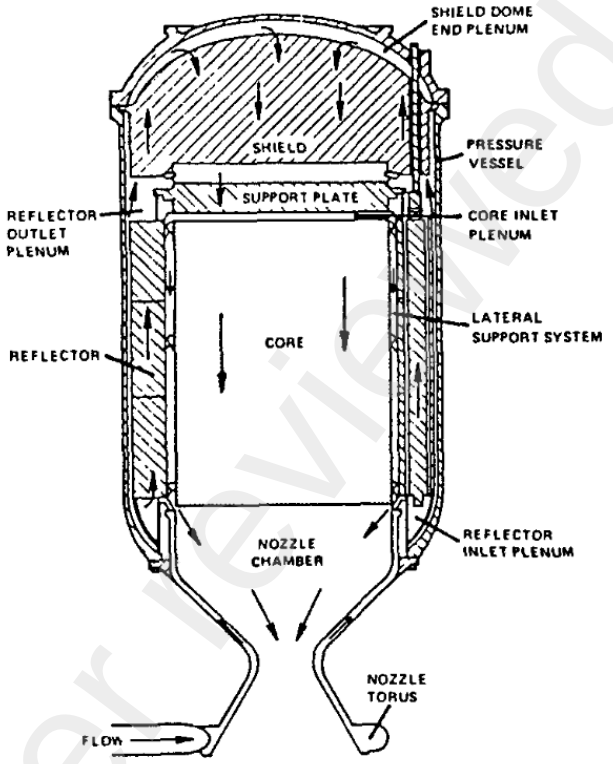

Figure 2: Reactor subsystem flow paths through the shield, support plate, reflector, core, and nozzle. Sourced from [10].

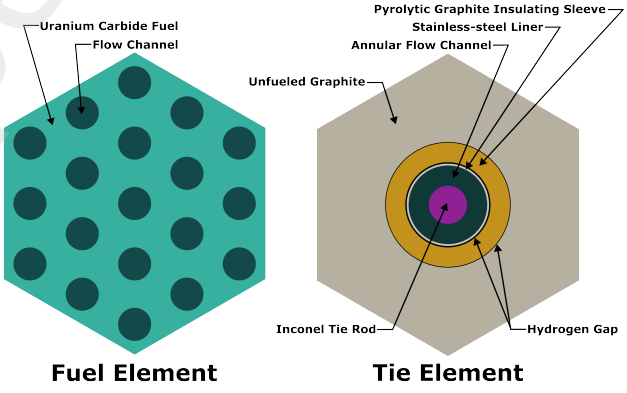

Figure 3: Fuel-element and tie-element cross sections.

A typical cluster places approximately six fuel elements around each central tie element. The support block at the nozzle end and the upper support plate maintain alignment and transmit axial loads, while the element bores and tie-tube annuli define the principal core coolant paths, as shown in Figure 4.

2.3. Reflector and Shield Cooling

The reflector surrounds the active core and increases neutron economy by returning leakage neutrons to the fuel region. The inner reflector/lateral support region includes graphite and support structures adjacent to the core, while the outer radial reflector is primarily beryllium and contains the control drum assemblies. Reflector coolant passages

This preprint research paper has not been peer reviewed. Electronic copy available at: https://ssrn.com/abstract=7593512

Table 1
Thermal-hydraulic model summary.

Region	Fluid Model	Solid Model	Heat Transfer	Assumptions
Core	1D equivalent (core-wide average)	3D heat conduction	Convection + radiation	Uniform radial temperature profile
Shield	1D equivalent channel	-	Convection + imposed heat flux	Uniform heat deposition
Reflector	1D equivalent (5 parallel channels)	2D cylindrical heat conduction	Convection + radiation	No core-reflector heat transfer

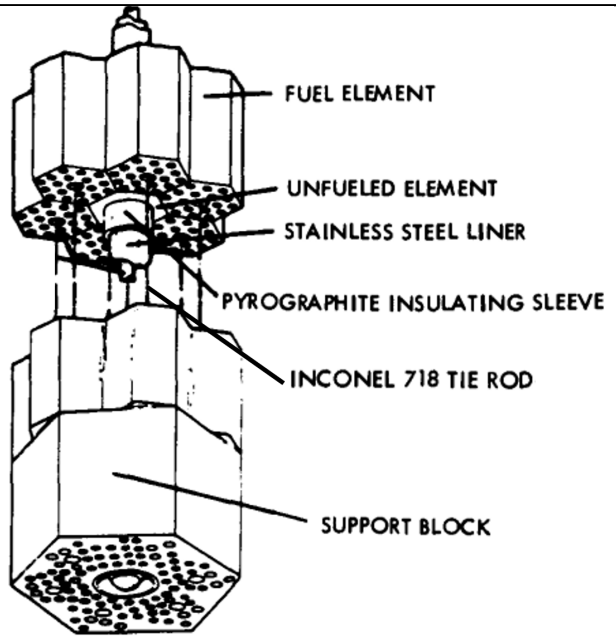

Figure 4: Fuel cluster and support block assembly. Sourced from [7].

remove local nuclear heating and help keep reflector temperatures within design limits. Figure 5 illustrates the reflector layout, including the discrete coolant channels distributed throughout the inner and outer reflector regions.

The upper shield and core support plate sit above the active core. The shield reduces radiation streaming toward the upper engine hardware and contains coolant flow to control thermal gradients. The core support plate anchors the tie rods, transfers core loads to the surrounding structure, and separates the shield dome/end plenum from the core inlet region. For the present model, these regions are important mainly as heat-generation, and pressure-loss.

3. Thermal-Hydraulics Model Development

The thermal-hydraulic model of the XE-Prime reactor is developed to simulate reactor-level flow and heat transfer from the reflector inlet to the core outlet. A schematic of the modeled system is shown in Figure 6.

The model is divided into three primary regions: the reflector, shield, and core. As summarized in Table 1, each region is represented using a combination of modeling approaches: one-dimensional equivalent fluid channels to capture convective heat transfer, two-dimensional cylindrical heat structures to approximate radial and axial conduction in non-core regions, and full three-dimensional heat conduction within the core to resolve detailed temperature distributions.

The modeling approach varies by region to balance physical fidelity and computational efficiency. The core is treated with the highest level of detail due to its strong coupling between heat generation and fluid flow, while reduced-order representations are used in the reflector and shield where thermal gradients are less complex.

The computational domain is bounded by inlet conditions at the reflector and outlet conditions at the core exit. A bleed flow boundary condition is also included to represent mass diverted from the core to drive the turbine. Modeling of downstream components, including the nozzle and full system integration, is reserved for future work.

Several additional simplifying assumptions are applied throughout the thermal-hydraulic model. The outer wall of the reactor pressure vessel is treated as adiabatic, and adiabatic boundary conditions are imposed at the core inlet and outlet surfaces for solid heat conduction. Minor pressure losses at the core outlet are assumed negligible relative to distributed frictional and form losses within the core and reflector flow paths. These assumptions are considered reasonable for the present analysis and are not expected to significantly impact the predicted core thermal response.

Figure 6 provides an overview of the complete thermal-hydraulic model, including flow paths, heat structures, and boundary conditions. Each region is described in detail in the following sections.

3.1. Governing Equations

The standard MOOSE THM formulation was used for the conservation of mass, momentum, and energy in the flow channels. MOOSE THM models one-dimensional, single-phase, compressible flow in ducts of variable cross-section and supports coupling to heat-conduction models for the surrounding solid structures [11].

The present work did not modify the underlying MOOSE flow equations, junction models, or energy-equation implementation. User-specified inputs were limited to the reactor geometry, equivalent-channel parameters, boundary conditions, form-loss coefficients, power deposition, material properties, and heat-transfer-coefficient correlations.

Convective heat transfer between the coolant and solid structures was modeled using the standard MOOSE wall-heating form,

$$q'_{wall} = H_w P_{hf} (T_w - T_f) \tag{1}$$

where H_w is the convective heat transfer coefficient, P_{hf} is the heated perimeter, T_w is the wall temperature, T_f is the local bulk fluid temperature, and q'_{wall} is the linear heat transfer rate. In the coupled core calculation, the

This preprint research paper has not been peer reviewed. Electronic copy available at: https://ssrn.com/abstract=7593512

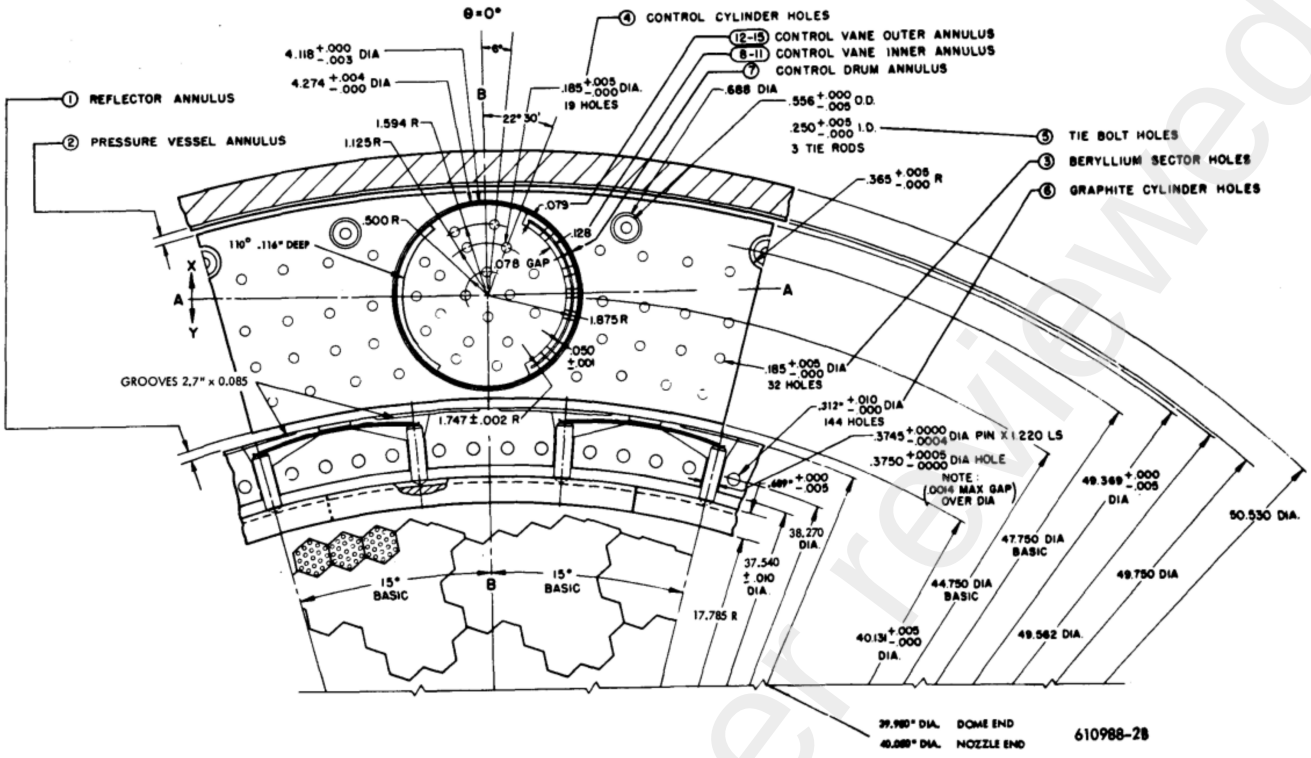

Figure 5: Cross section of the reflector region, including annuli, beryllium-sector holes, tie-bolt holes, and control drum geometry. Sourced from [7].

fluid model transfers coolant temperature and heat transfer coefficient fields to the heat-conduction model, while the heat-conduction model returns wall temperatures to the fluid model. This is consistent with the MOOSE *HeatTransferFromExternalAppTemperature1Phase* component, which adds wall heating to the one-phase energy equation using an externally supplied wall temperature.

The heat transfer coefficient (HTC) is obtained from the Nusselt number:

$$H_w = \frac{Nu\, k}{D_h} \tag{2}$$

where H_w is the heat transfer coefficient, Nu is the Nusselt number, k is the fluid thermal conductivity, and D_h is the hydraulic diameter.

Turbulent pipe flow in the core, shield, and reflector channels is modeled using the Lucier correlation [12]. This correlation was selected to maintain consistency with previous thermal-hydraulic modeling studies of nuclear thermal propulsion reactors [12], thereby facilitating comparison of results with existing work. Annular flow within the tie channel is modeled using a Gnielinski-type correlation with annular-flow corrections [13]. The full formulations of both correlations are presented in Appendix A.

The Darcy friction factor is computed using the Churchill correlation, using the default *WallFrictionChurchillMaterial*. The full Churchill friction-factor formulation is provided in Appendix A.

Frictional pressure losses were computed using the MOOSE Churchill wall-friction material. Additional local or distributed losses were applied using MOOSE form-loss components. The flow conditions considered in this work were confirmed to lie within the applicable ranges of the selected heat-transfer and friction-factor correlations, ensuring that the empirical models were applied within their intended domains of validity. In MOOSE, the form-loss input K' is defined as a loss coefficient per unit length, so an equivalent localized loss K distributed over a short length L satisfies $K' = K/L$.

Volumetric heat generation was applied in the reflector and pressure-vessel heat structures according to prescribed power fractions and axial power shape. Shield heating was represented as direct volumetric heat addition to the shield coolant channel. Radiative heat transfer was included between selected reflector and vessel heat structures using the MOOSE heat-transfer module, which supports heat conduction, convection, and gray/diffuse surface radiation.

3.2. Boundary Conditions

Boundary conditions are applied at the system level to define inlet, outlet, and bleed flow behavior.

A temperature and mass flow rate boundary condition is specified at the reflector inlet. A pressure outlet boundary condition is applied at the core outlet. A separate mass flow rate and temperature boundary condition is used for the bleed outlet to represent flow diverted to the turbine.

This preprint research paper has not been peer reviewed. Electronic copy available at: https://ssrn.com/abstract=7593512

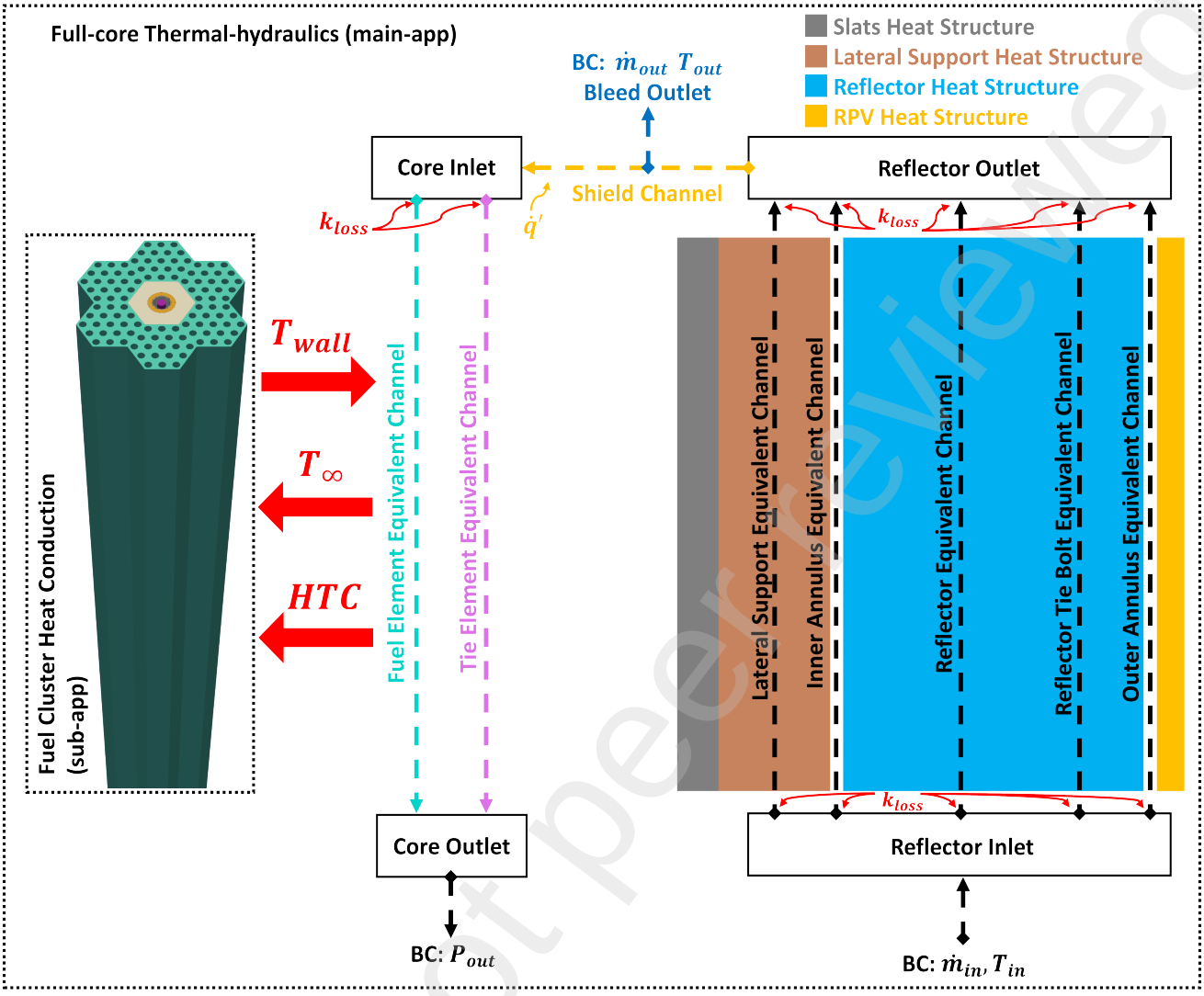

Figure 6: Thermal-hydraulics model diagram.

For steady-state simulations, boundary conditions are applied as constant values. For transient simulations, time-dependent boundary conditions are prescribed using *ControlLogic* functions derived from external CSV data.

3.3. Core Thermal-Hydraulic Model

The reactor core is modeled using a coupled approach that combines three-dimensional heat conduction with one-dimensional equivalent fluid channels. As summarized in Table 2, this hybrid representation captures detailed solid temperature distributions while maintaining a reduced-order description of coolant flow.

Previous studies have shown that radial heat transfer within the core is negligible due to the tailored inlet orifice diameters, which adjust mass flow rates to offset the radial power profile [12]. As a result, heat transfer within the core is predominantly axial, and a core-averaged fluid representation is appropriate.

As shown in Table 2, the core model separates the solid and fluid physics while coupling them through conjugate heat transfer. The solid domain resolves detailed temperature fields within a representative fuel cluster, while the fluid channels capture the bulk thermal-hydraulic behavior using equivalent flow paths.

3.3.1. Heat Conduction

Heat conduction within the core is modeled using the MOOSE heat conduction module. A single representative fuel cluster is constructed, consisting of one unfueled central element (tie tube) surrounded by six fuel elements.

Figure 3 illustrates the geometry and material composition of the fuel elements and tie tube, while Figure 7 shows the corresponding heat conduction mesh and coupling boundaries. Three wall surfaces are coupled to the thermal-hydraulic model: the fuel channel wall, the inner tie channel wall, and the outer tie channel wall.

This preprint research paper has not been peer reviewed. Electronic copy available at: https://ssrn.com/abstract=7593512

Table 2
Core modeling summary.

Component	Model Type	Description	Dominant physics & models
Solid domain	3D heat conduction	Representative fuel cluster (1 tie element + 6 fuel elements)	Volumetric heating, radiation, temperature dependent solid properties
Fuel channel	1D equivalent channel (pipe flow)	Represents hydrogen flow in fuel elements	Lucier HTC, Churchill friction factor
Tie channel	1D equivalent channel (annular flow)	Represents hydrogen flow in tie tubes	Gnielinski HTC, Churchill friction factor
Coupling	Conjugate heat transfer	Fluid-solid coupling via wall temperature exchange	HTC-based convective heat transfer (temperature-driven)

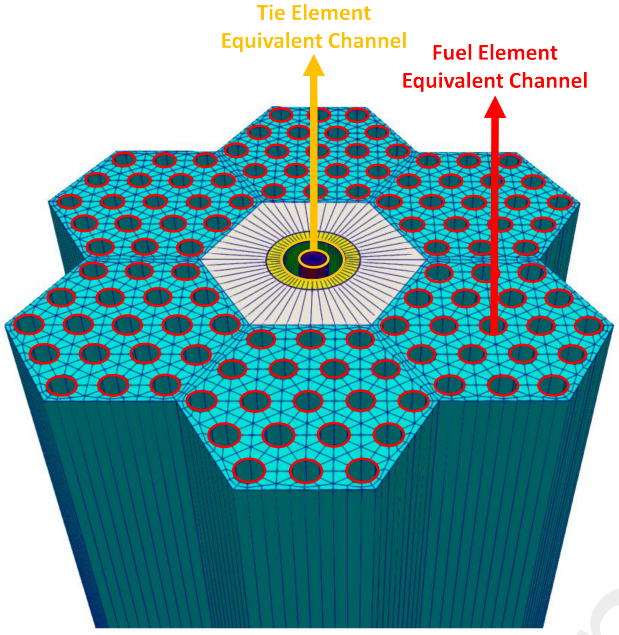

Figure 7: Fuel cluster heat conduction mesh and wall coupling boundaries.

Radiative heat transfer is modeled between the tie wall and stainless steel wall using an emissivity of 0.3. Hydrogen gaps between the stainless steel liner, pyrolytic graphite insulating sleeve, and moderator block are approximated using solid materials with equivalent thermal properties. All material interfaces assume perfect thermal contact.

The external boundaries of the computational domain use the default natural boundary condition in MOOSE, corresponding to zero normal heat flux (adiabatic boundaries). Axial and radial thermal expansion are not considered in this model.

Volumetric power generation is applied based on power fractions from Monte Carlo neutronics simulations of the XE-Prime reactor core, as listed in Table 3, with the core axial power shape from the XE-1 design report shown in Figure 8.

Table 3
Fuel cluster power fractions.

Material	Power Fraction
Fuel element (UC_2)	0.968322
Unfueled Graphite	0.0096707
Pyrographite	0.0014452
Stainless Steel	0.0003549
Tie Rod (Inconel)	0.0008662

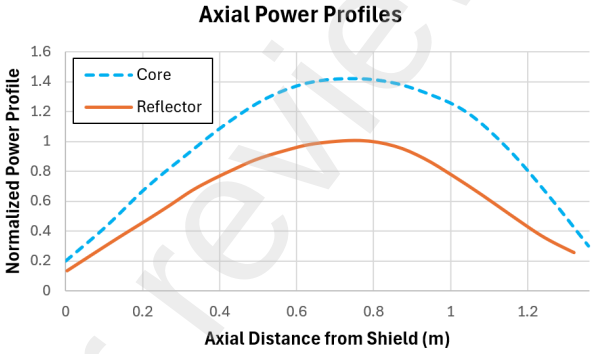

Figure 8: Axial power profiles for the core and reflector regions. Sourced from [7].

3.3.2. Equivalent Core Channels

The core flow is represented by two equivalent channels: a fuel channel and a tie channel, with parameters summarized in Table 4. These channels are connected in parallel between a core inlet and core outlet plenum.

For each channel type, the equivalent hydraulic diameter was given simply as the hydraulic diameter of a single channel.

The equivalent flow area (A_{eq}) is given by:

$$A_{eq} = A_{ch} \times N_{ch} \tag{3}$$

where A_{ch} is the single channel flow area and N_{ch} is the total number of physical channels represented.

The equivalent heated perimeter $(P_{h,\,eq})$ is given by:

$$P_{h,\,eq} = P_{h,\,ch} \times N_{ch} \tag{4}$$

where $P_{h,\,ch}$ is the single channel heated perimeter.

The fluid channels are thermally coupled to the solid domain through the wall boundaries. At each axial location, the fluid model provides a convective heat transfer coefficient and bulk fluid temperature to the solid model, while the solid model returns wall temperatures. These quantities are used to compute the local heat flux based on the defined heated perimeter, ensuring conservation of energy between the fluid and solid domains. No scaling is applied in the coupling, as the exchanged quantities are cross-sectionally averaged and therefore independent of geometric differences between the fluid and solid models.

Localized pressure losses are modeled using K-loss factors to represent inlet, outlet, and other minor losses and to

Preprint not peer reviewed
This preprint research paper has not been peer reviewed. Electronic copy available at: https://ssrn.com/abstract=7593512

Table 4
Equivalent core channel parameters.

Parameter	Equivalent fuel channel	Equivalent tie channel
Channel geometry	Circular pipe	Annulus
Single channel radius	1.2095 mm	Inner: 1.397 mm Outer: 2.870 mm
Single channel flow area	4.596 mm^2	19.746 mm^2
Single channel heated perimeter	7.600 mm	Inner: 8.778 mm Outer: 18.033 mm
Number of channels per element	19	1
Number of elements	1584	289
Total number of physical channels represented	30,096	289
Equivalent flow area	0.13833 m^2	0.0057065 m^2
Equivalent heated perimeter	228.724 m	Inner: 2.5367 m Outer: 5.2115 m
Equivalent hydraulic diameter	2.419 mm	2.946 mm
Length (m)	1.32	1.32
Applied inlet K-loss coefficient	9250	9750
HTC correlation	Lucier turbulent pipe correlation	Gnielinski annular correlation
Friction factor correlation	Churchill	Churchill

Table 5
Reflector region heat structure geometry, material definition, and power fractions.

Parameter	Slats	Lateral Support	Outer Reflector	RPV
Inner radius (cm)	45.060	46.711	51.029	63.210
Outer radius (cm)	46.609	50.805	62.687	65.532
Length (m)	1.359	1.359	1.359	1.359
Bulk material	Graphite	Graphite	Beryllium	Aluminum
Power fraction	0.002172	0.004952	0.008858	0.001046

enforce the correct flow split between the fuel and tie channels. Distributed wall-friction losses within the channels are computed separately using the Churchill friction-factor correlation. Because MOOSE applies K-losses uniformly over the length of a component, short auxiliary segments are introduced between the inlet plenum and the core channels so that the localized losses are distributed over a short distance, providing a close approximation to concentrated losses.

3.4. Shield and Reflector

The shield and reflector regions are modeled using one-dimensional equivalent fluid channels coupled to heat conduction models. In contrast to the core, these regions are represented using simplified approaches, as heat transfer is less strongly coupled to local power generation and detailed three-dimensional effects are less significant.

3.4.1. Reflector Heat Structures

The reflector solid region, as shown in Figure 5 and Figure 6, is represented by four cylindrical heat structures: the graphite slats, lateral support, outer reflector, and reactor pressure vessel (RPV). Volumetric power generation is applied to each structure based on power fractions obtained from Monte Carlo simulations. These power fractions are held constant for all evaluated state points and are scaled only by the total reactor power level.

The geometry, material properties, and power fractions for these structures are listed in Table 5.

Radiative heat transfer is included between reflector components with emissivity of 0.7. However, radiation heat transfer between the core and reflector, as well as between the reflector and the external environment, is neglected. Additionally, since core heat transfer is assumed to be primarily axial, heat transfer between the graphite slats and the core is not modeled.

3.4.2. Reflector Equivalent Channels

As shown in Figure 6, the reflector region is modeled using five equivalent flow channels connected in parallel between the reflector inlet and outlet plenums, with parameters summarized in Table 6. The values were taken from the TNT model in the XE-1 design report [7], as they were based on complex geometries and these were the most accurate equivalent channel values available.

All reflector channels use the Lucier correlation for heat transfer coefficient calculations and the Churchill correlation for friction factor. K-loss factors are applied uniformly and tuned to achieve the correct pressure drop and flow distribution among the channels.

The channels are thermally coupled to the surrounding heat structures through wall boundaries using the *HeatTransferFromHeatStructure1Phase* component. In this formulation, wall temperatures are obtained directly from the associated heat structure, and convective heat transfer is computed using the local heat transfer coefficient and bulk fluid temperature. This provides a consistent, temperature-based conjugate heat transfer coupling between the fluid channels and solid regions.

The inner and outer annulus channels are coupled to the corresponding bounding surfaces of the reflector heat structures. The inner reflector channel is coupled to an internal boundary centered within the inner reflector heat structure, while the outer reflector tie channel is coupled to an internal boundary located at its corresponding radial position. The outer reflector channel is coupled to the outer reflector structure at multiple locations using four distinct internal boundaries. This multi-boundary approach preserves

This preprint research paper has not been peer reviewed. Electronic copy available at: https://ssrn.com/abstract=7593512

Table 6
Reflector equivalent channel parameters.

Parameter	Inner annulus	Inner reflector channel	Outer reflector channel	Outer reflector tie channel	Outer annulus
Number of physical channels represented	1	144	1677	36	1
Single channel flow area (cm^2)	71.742	0.4946	0.1716	0.3165	206.838
Single channel heat transfer area (m^2)	8.69	0.03387	0.01995	0.02709	10.74
Equivalent flow area (m^2)	0.007174	0.007122	0.028779	0.0011395	0.020684
Hydraulic diameter (mm)	4.481	7.938	4.676	6.350	10.465
Equivalent Heated perimeter (m)	6.395	3.589	24.618	0.718	7.906
Length (m)	1.359	1.359	1.359	1.359	1.359
Applied inlet K-loss coefficient	6	5E-6	3	2.5E-4	25
HTC correlation	Lucier	Lucier	Lucier	Lucier	Lucier
Friction factor correlation	Churchill	Churchill	Churchill	Churchill	Churchill

the effective thermal resistance associated with coolant passage spacing, although some approximation remains due to geometric asymmetry introduced by the control drums.

3.4.3. Shield Equivalent Channel

The shield region is represented by a single equivalent flow channel connected between the reflector outlet plenum and the core inlet plenum. The channel parameters are provided in Table 7.

Table 7
Shield equivalent parameters.

Parameter	Shield Equivalent Channel
Flow area	0.041161 m^2
Hydraulic diameter	12.70 mm
Length	0.5701 m
Friction factor	Churchill

A bleed channel is included to represent flow diverted from the core to drive the turbine. A volumetric heat source is applied to the shield channel to account for heat deposition from the shield and core support plate, based on the prescribed shield power fraction.

3.5. Solid Properties

Solid material properties were specified for the core heat-conduction mesh and the reflector/pressure-vessel heat structures. In both models, density is treated as constant within each material region, while thermal conductivity and specific heat are temperature dependent. All temperatures in the material-property functions are in Kelvin, thermal conductivity is in W/m-K, specific heat is in J/kg-K, and density is in kg/m^3. The material properties are summarized in Table 8 and are obtained from the NERVA program Material Properties Data Books [14, 15].

Table 8
Solid material property assignments and corresponding thermophysical properties.

Material	Density (kg/m^3)	Thermal Conductivity (W/m-K)	Specific Heat (J/kg-K)
Uranium Carbide	12,675	Eq. (B.1)	Eq. (B.2)
Graphite	1,850	Eq. (B.3)	Eq. (B.4)
Pyrolytic Graphite	2,215	Figure 20(a)	Figure 20(b)
Stainless Steel	7,500	Eq. (B.5)	Eq. (B.6)
Hydrogen-gap	2.42	0.23	14.5
Inconel	8,221	Figure 20(c)	422.8
Beryllium	1689.3	Figure 20(d)	1863.13
Aluminum	2669.5	205	897

The full polynomial property functions and material-property graphs referenced in Table 8 are provided in Appendix B.

3.6. Fluid Properties

Thermophysical properties of hydrogen are modeled as functions of temperature and pressure using tabulated data obtained from the NIST database [16]. Properties are implemented through bicubic interpolation in pressure–temperature (P–T) space [17].

To ensure consistency with the energy-based formulation used in MOOSE-THM, an inverse Newton solver is employed to map interpolated properties into specific volume–internal energy (v–e) space. This transformation enables evaluation of fluid properties in terms of the primary solution variables.

Although the model spans operating conditions of approximately 17–2500 K and 1–6 MPa, the thermodynamic path followed during the calculation remains in the single-phase hydrogen region. During the cryogenic portion of the operating path, the pressure remains above the hydrogen critical pressure, and the fluid transitions continuously into the supercritical regime as it is heated. Near the pseudo-critical region (approximately 40 K, depending on pressure), hydrogen exhibits strong property gradients, including a rapid decrease in density and a peak in specific heat capacity. To improve numerical robustness, thermophysical properties below approximately 40 K were smoothed while preserving the overall trends.

These steep gradients can lead to poor numerical conditioning and convergence difficulties in the inverse Newton solver. To improve robustness, fluid properties below 40 K

Preprint not peer reviewed

This preprint research paper has not been peer reviewed. Electronic copy available at: https://ssrn.com/abstract=7593512

were artificially smoothed to reduce gradients in the pseudo-critical region.

As a result, the model uses physically accurate property data from approximately 40 K to 2500 K, while properties in the range of 17–40 K are numerically stabilized but not strictly physical. This approximation has a negligible impact on results due to the limited portion of the transient below these conditions.

Additionally, the NIST database assumes molecular hydrogen (H_2) across the full temperature range. Effects associated with high-temperature dissociation into atomic hydrogen (H), which may become significant at elevated temperatures, are not included in this model [18–20].

4. Design-Prediction Benchmark Methodology

Steady-state design-prediction benchmarking is performed using model-to-model comparison against the XE-1 nuclear and thermal design report, providing a reference solution for quantities that were not directly measured in experiments. The XE-1 design report provides a detailed steady-state model at the full-power operating condition of 1120 MW [7]. This model includes detailed thermal-hydraulic behavior and serves as a consistent reference for the shared core design used in XE-1, XE-2, and XE-Prime.

4.1. Benchmark Quantities

Comparisons are performed at 1120 MW with emphasis on axial distributions of key thermal-hydraulic quantities, including pressure, temperature, density, Reynolds number, and heat transfer characteristics. Agreement in these quantities provides confidence that the MOOSE implementation reproduces the historical design-prediction behavior of the reactor model.

The fuel-element comparison includes fuel-channel pressure, wall and gas temperature, gas density, Reynolds number, heat flux, heat transfer coefficient, and average solid fuel temperature. The tie-element comparison includes tie-channel pressure, gas temperature, wall temperature, and average tie-block temperature. These quantities were selected because they test the hydraulic response, heat transfer implementation, thermodynamic property treatment, and solid/fluid coupling used in the model.

4.2. Importance for Neutronics Coupling

The benchmarked quantities are also important for future neutronics coupling. Fuel temperature is a dominant solid-temperature feedback quantity, and hydrogen temperature and density define moderation and additional feedback in the coolant channels. The tie-channel gas temperature is particularly important because it directly governs hydrogen density in the tie channel. Given that hydrogen density was not explicitly reported in the XE-1 model, close agreement in gas temperature provides confidence that the MOOSE model is capturing the key thermodynamic behavior relevant to neutronic feedback.

5. Results and Benchmarking

5.1. Fuel Element Comparison

The following results correspond to the fuel element model in the XE-1 design report [7].

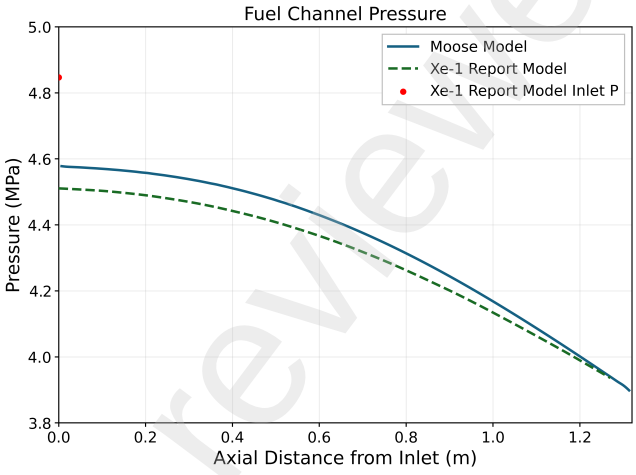

Figure 9: Fuel channel pressure vs axial position.

As shown in Figure 9, both models predict a smooth, monotonic pressure drop along the channel. The MOOSE model consistently yields slightly higher pressures than the XE-1 model, indicating minor differences in friction factor or property evaluation. The agreement improves toward the outlet, suggesting that both models capture the overall hydraulic behavior well.

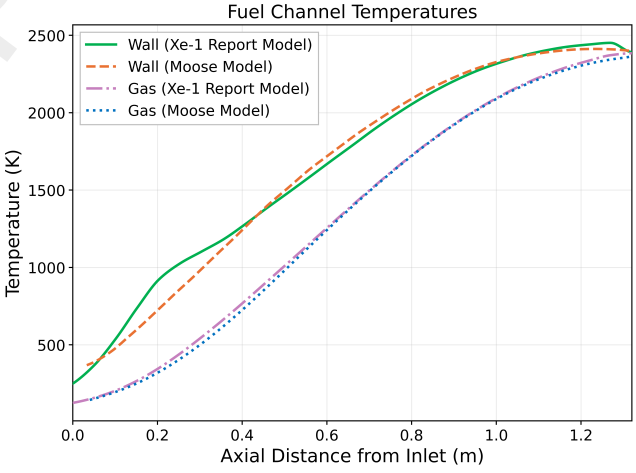

Figure 10: Fuel channel wall and gas temperature vs axial position.

In Figure 10, both models capture the expected increase in gas and wall temperatures along the channel, as well as the temperature difference between the wall and bulk gas. A mild inflection near the inlet region (~0.2 m) is observed in the XE-1 results, suggesting the presence of inlet flow conditions or turbulent mixing effects not explicitly modeled.

This preprint research paper has not been peer reviewed. Electronic copy available at: https://ssrn.com/abstract=7593512

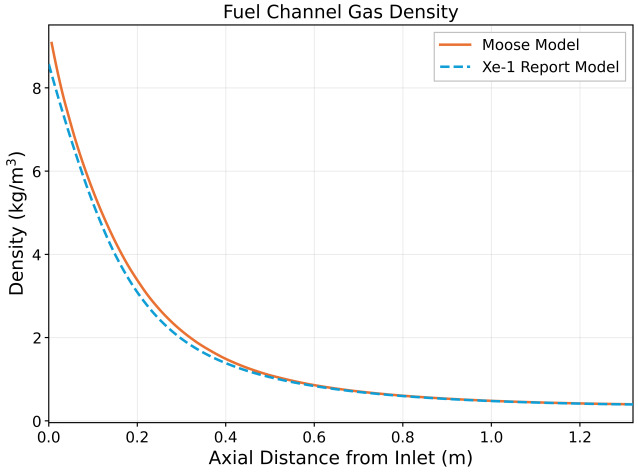

Figure 11: Fuel channel hydrogen density vs axial position.

As shown in Figure 11, both models exhibit a strong decrease in gas density along the channel due to heating and thermal expansion. Agreement is excellent overall, with minor deviations near the inlet. Downstream convergence indicates consistent thermodynamic behavior between models.

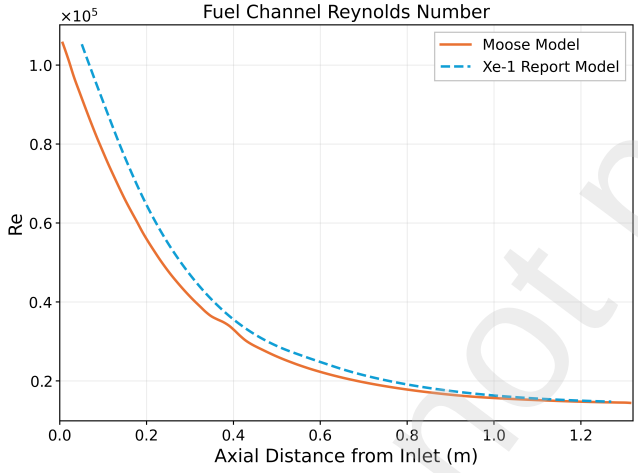

Figure 12: Fuel channel Reynolds number vs axial position.

In Figure 12, both models predict a decreasing Reynolds number along the channel, consistent with the reduction in density and changes in fluid properties. The MOOSE model produces slightly lower Reynolds numbers across most of the channel, reflecting small differences in density and/or viscosity. The agreement improves in the downstream region.

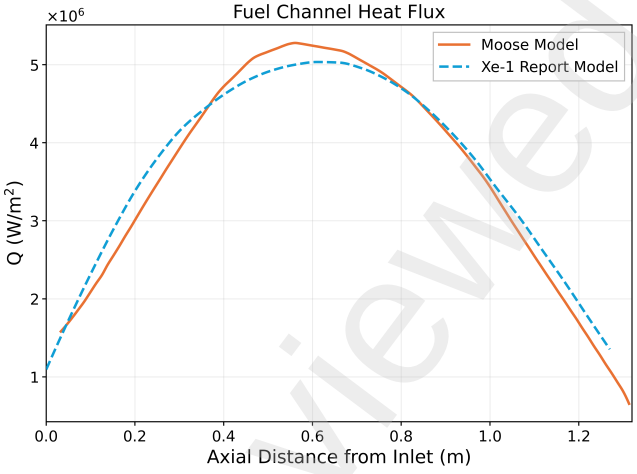

Figure 13: Fuel channel heat flux vs axial position.

Figure 13 shows that both models reproduce the expected cosine-like axial heat flux profile, with a peak near the channel midpoint (~0.5–0.6 m). The MOOSE model predicts a slightly sharper peak and marginally lower values near the outlet, but overall agreement confirms consistent implementation of the axial power distribution.

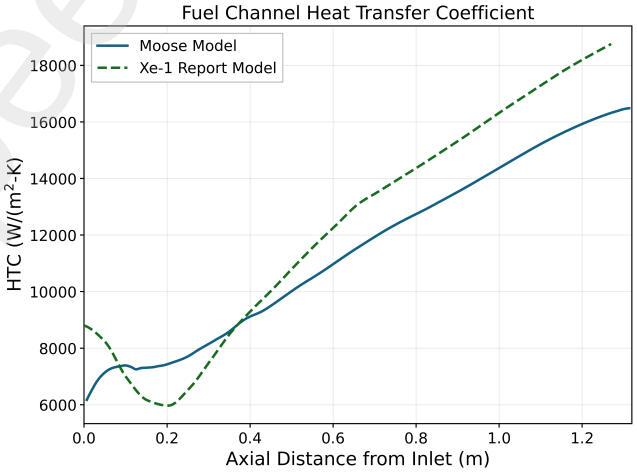

Figure 14: Fuel channel heat transfer coefficient vs axial position.

As illustrated in Figure 14, both models predict an increasing heat transfer coefficient along the channel. A notable discrepancy occurs near the inlet (~0–0.3 m), where the XE-1 model exhibits a dip followed by recovery (a "hump"), while the MOOSE model predicts a smoother trend. This behavior is likely associated with inlet turbulence, flow development, or non-uniform inlet conditions present in the XE-1 model but not explicitly captured in the MOOSE formulation.

Preprint not peer reviewed

This preprint research paper has not been peer reviewed. Electronic copy available at: https://ssrn.com/abstract=7593512

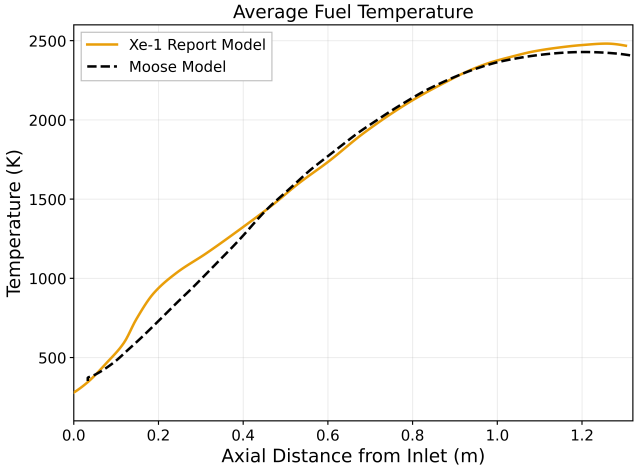

Figure 15: Average fuel temperature vs axial position.

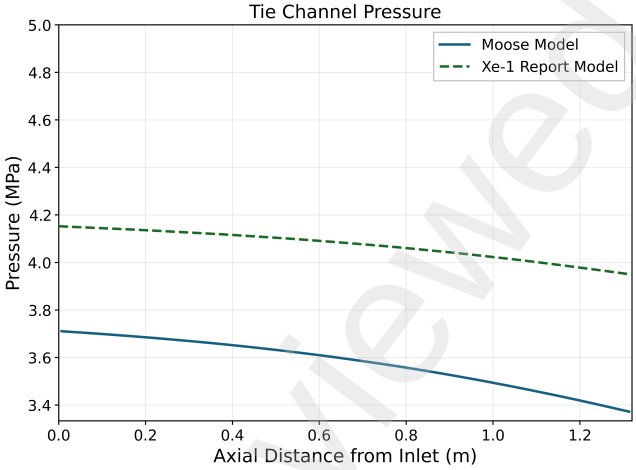

Figure 16: Tie channel pressure vs axial position.

Finally, Figure 15 shows the resulting average fuel temperature distribution. The axial average fuel temperature represents the cross-sectionally averaged (volume-weighted) fuel temperature at each axial location along the fuel element. Both models predict the expected monotonic increase and outlet plateau. The MOOSE model slightly underpredicts temperatures in the core outlet region. Differences near the inlet can be traced back to discrepancies in HTC and gas temperature behavior (see Figure 10 and Figure 14), indicating that fuel temperature variations are driven by upstream thermal-hydraulic differences rather than independent model behavior.

Across Figure 9 through 15, the MOOSE model reproduces the dominant fuel-element axial trends reported by the XE-1 design calculation. The largest discrepancies consistently occur near the inlet region (~0.2 m), where the XE-1 model exhibits localized features, most notably the temperature and heat transfer coefficient "hump" (Figure 10 and Figure 14), likely driven by turbulent inlet conditions and flow development effects not explicitly modeled.

5.2. Tie Element Comparison

The following results correspond to the tie element model in the XE-1 design report.

As shown in Figure 16, both models predict a gradual pressure decrease along the tie channel. The MOOSE model consistently underpredicts pressure relative to the XE-1 model across the entire axial length. This discrepancy likely arises from differences in the assumed hydraulic losses, junction/mixing losses, and the effective location of the outlet pressure boundary condition in the reduced-order 1D representation. The prescribed outlet pressure is applied downstream of the tie/fuel channel mixing region, so the channel outlet pressures are not directly forced to match the boundary value at the last internal channel location.

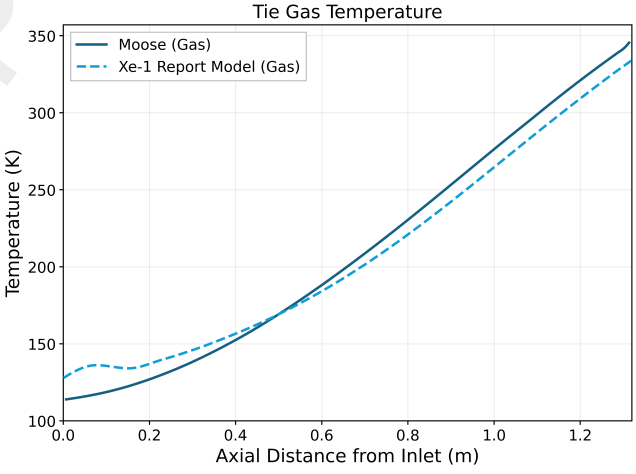

Figure 17: Tie channel gas temperature vs axial position.

Figure 17 shows strong agreement between the MOOSE and XE-1 models for tie channel gas temperature. Both models predict a smooth, monotonic temperature increase along the channel, with only minor deviations throughout the axial length. This agreement is particularly important, as gas temperature is the primary driver of hydrogen density in the tie channel. Given that the XE-1 report does not provide modeled hydrogen density values, this close agreement provides confidence that the MOOSE model is capturing the key thermodynamic behavior relevant to neutronic feedback.

Preprint not peer reviewed

This preprint research paper has not been peer reviewed. Electronic copy available at: https://ssrn.com/abstract=7593512

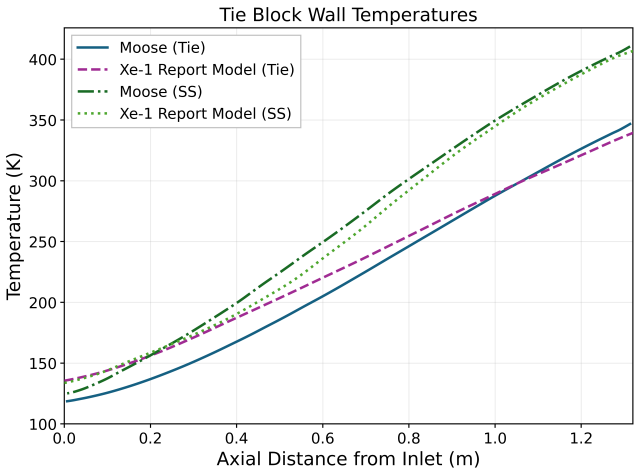

Figure 18: Tie channel wall temperature vs axial position.

As illustrated in Figure 18, the models show similar trends in wall temperature increase along the channel, but with noticeable deviations in magnitude. The MOOSE model generally predicts slightly lower tie wall temperatures compared to the XE-1 model, particularly in the inlet to mid regions. Despite these differences, the overall shape and progression are consistent, indicating similar heat transfer behavior even if local heating differs.

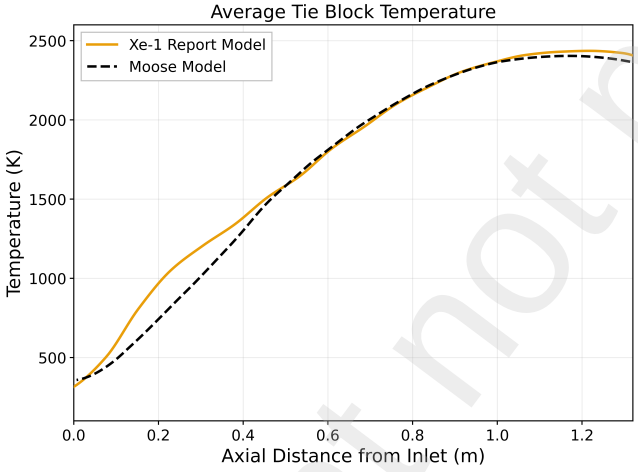

Figure 19: Average tie block temperature vs axial position.

In Figure 19, both models predict the expected increase in average tie block temperature along the channel, with strong agreement in overall trend and outlet values. Minor deviations appear in the inlet region and mid-channel, consistent with differences observed in average fuel temperature (Figure 15). These differences do not significantly impact the overall thermal response.

Across Figures 16 through 19, the MOOSE model demonstrates generally good agreement with the XE-1 design report model for tie channel behavior. While some discrepancies are observed, the agreement in tie gas temperature and solid temperature (Figures 17 and 19) is particularly strong.

This is a critical result, as tie channel gas temperature directly governs hydrogen density, which is an important neutronic feedback parameter. Given that hydrogen density was not explicitly reported in the XE-1 model, the close agreement in gas temperature provides confidence that the MOOSE model is accurately capturing the relevant physics for neutronic feedback, even in the presence of minor discrepancies.

5.3. Discussion

The design-prediction benchmark confirms that the MOOSE thermal-hydraulic model reproduces the dominant axial trends reported in the XE-1 design calculations. The fuel-channel comparisons verify the pressure-drop behavior, thermal expansion of hydrogen, axial heat-flux distribution, convective heat-transfer implementation, and coupled fuel-temperature response. The tie-channel comparisons verify the reduced annular-channel representation and demonstrate that gas temperature and average solid temperature are captured with sufficient fidelity for future feedback applications.

Remaining discrepancies are localized primarily near the inlet region of the fuel channel, where the XE-1 model exhibits features that are not reproduced by the present equivalent-channel approach. These deviations are consistent with inlet turbulence, developing flow, non-uniform inlet conditions, or details of the historical design calculation that are not explicitly represented in the MOOSE model. Downstream convergence in pressure, density, Reynolds number, and temperature indicates that the integrated axial thermal-hydraulic response is captured for the purposes of the Part I design benchmark.

Because this paper focuses on a design-prediction benchmark, the comparisons do not yet evaluate measured full-system transient response. Experimental EP-5C steady-state and transient validation are reserved for Part II of this paper series [1].

6. Model Limitations

Several modeling assumptions and simplifications introduce limitations in the predictive capability of the thermal-hydraulic model. The shield and core support plate are modeled using simplified representations, which may impact predicted temperatures and heat deposition in these regions. The reflector is also simplified through equivalent flow channels and cylindrical heat structures. Radiation heat transfer between the core and reflector, as well as between the reflector and the external environment, is neglected. This assumption is considered reasonable because the primary heat-transfer mechanisms in these regions are conduction through solid components and convection to the hydrogen coolant. In addition, the effective radiative exchange areas and temperature differences between adjacent components are relatively small, limiting the contribution of thermal radiation to the overall heat transfer.

The core flow is represented with core-wide equivalent fuel and tie channels. Previous studies support the assumption that radial heat transfer within the core is negligible

This preprint research paper has not been peer reviewed. Electronic copy available at: https://ssrn.com/abstract=7593512

due to orificing, but the model does not resolve element-by-element radial power, mass-flow, or temperature variations. The approach is therefore best interpreted as a core-averaged representation of the dominant axial thermal-hydraulic behavior rather than a full core-resolved subchannel model.

Thermal expansion is not modeled, and therefore coupling between geometric changes, flow area, and reactivity is not captured. Material degradation effects such as fuel cracking, corrosion, and niobium coating loss are not explicitly modeled. These effects are important for future fuel performance applications but are outside the scope of the present work.

Hydrogen thermophysical properties are modified below approximately 40 K to maintain numerical stability, resulting in nonphysical behavior at low temperatures. At high temperatures, hydrogen dissociation is not modeled, which may affect predictions at the highest power conditions. The modeled reactor-level domain is treated as single-phase hydrogen, and two-phase behavior upstream or downstream of the modeled domain is outside the present model.

7. Conclusion

A high-fidelity thermal-hydraulic MOOSE model of the XE-Prime reactor was developed and benchmarked against historical design calculations from the XE-1 design report. The model represents the core, reflector, and shield using coupled one-dimensional flow channels, reduced-order heat structures, and detailed three-dimensional heat conduction within a representative fuel cluster.

Steady-state thermal-hydraulic predictions show close agreement with the XE-1 design report. Fuel-channel predictions reproduce the expected pressure drop, hydrogen heating, density decrease, Reynolds number trend, heat-flux distribution, heat-transfer-coefficient trend, and solid fuel temperature profile. Tie-channel predictions similarly reproduce the pressure trend, gas temperature, wall temperature, and average tie-block temperature with generally good agreement. Agreement in hydrogen density, gas temperature, and solid temperature is particularly important for subsequent coupled analyses because these quantities govern thermal and hydrogen-density reactivity feedback.

The results of this Part I study establish a design-benchmarked thermal-hydraulic representation of the XE-type reactor and provide the model-development basis for experimental validation. The companion Part II study [1] evaluates the same thermal-hydraulic model against measured steady-state and transient data from the XE-Prime EP-5C full-power experiment. Together, the internal design-prediction benchmark presented here and the experimental validation presented in Part II establish a historically anchored thermal-hydraulic model for subsequent NTP transient, neutronic, and fuel-performance analyses.

8. Future Work

Several areas for future work were identified during the development and benchmarking of the XE-Prime model. First, the Part I design-prediction benchmark presented here should be extended to experimental validation against EP-5C steady-state hold points and transient measurements. That validation is the focus of Part II of this paper series.

Second, coupling the thermal-hydraulic model to neutronics would enable evaluation of fuel-temperature and hydrogen-density feedback during steady-state and transient operation. A validated thermal-hydraulic model provides the temperature, pressure, density, and flow fields needed by such a coupled multiphysics framework.

Third, coupling the model to fuel performance simulations would enable analysis of thermal expansion, fuel cracking, fuel loss, mid-band corrosion, and niobium coating degradation. These effects may also introduce additional thermal-hydraulic and neutronic feedback mechanisms that are not represented in the current model.

Finally, expansion of the thermal-hydraulic model to include the full NTP system, including the propellant tank, turbopump, turbine, feed system, and nozzle, would enable integrated analysis of system-level startup, shutdown, and operating behavior.

Preprint not peer reviewed

This preprint research paper has not been peer reviewed. Electronic copy available at: https://ssrn.com/abstract=7593512

A. Governing-Equation Correlation Formulations

This appendix lists the full formulation of the heat-transfer and friction-factor correlations referenced in Section 3.1.

A.1. Lucier turbulent pipe-flow heat-transfer correlation

For turbulent pipe flow in the fuel, shield, and reflector channels, the Lucier correlation [12] is used:

$$Nu = 0.0217\, Re^{0.8}\, Pr^{0.4} \left(\frac{T_w}{T}\right)^{-0.34} \tag{A.1}$$

A.2. Gnielinski-type annular heat-transfer correlation

For annular flow within the tie channel, a Gnielinski-type correlation with annular corrections [13] is used:

$$Nu_{common} = \frac{(f_{ann}/8)RePr}{k_1 + 12.7\sqrt{f_{ann}/8}\left(Pr^{2/3} - 1\right)} \left[1 + \left(\frac{D_h}{L_{core}}\right)^{2/3}\right] \tag{A.2}$$

where,

$$k_1 = 1.07 + \frac{900}{Re} - \frac{0.63}{1 + 10Pr} \tag{A.3}$$

$$f_{ann} = \left(1.8 \log_{10} Re^* - 1.5\right)^{-2} \tag{A.4}$$

$$Re^* = Re \frac{\left(1 + a^2\right) \ln a + \left(1 - a^2\right)}{(1 - a)^2 \ln a} \tag{A.5}$$

$$K_j = \left(\frac{T}{T_{w,j}}\right)^n, \qquad j \in \{i, o\}, \quad n = 0.34 \tag{A.6}$$

$$F_{ann} = \begin{cases} 0.75a^{-0.17}, & \text{inner wall,} \\ 0.9 - 0.15a^{0.6}, & \text{outer wall.} \end{cases} \tag{A.7}$$

Then the inner and outer annular wall Nusselt numbers are:

$$Nu_i = Nu_{common} \left(0.75a^{-0.17}\right) K_i \tag{A.8}$$

$$Nu_o = Nu_{common} \left(0.9 - 0.15a^{0.6}\right) K_o \tag{A.9}$$

where,

$$a = \frac{D_i}{D_o} \tag{A.10}$$

Preprint not peer reviewed

This preprint research paper has not been peer reviewed. Electronic copy available at: https://ssrn.com/abstract=7593512

A.3. Churchill friction-factor correlation

The Darcy friction factor is computed using the Churchill correlation, using the default *WallFrictionChurchillMaterial*, which implements the Churchill friction-factor correlation as:

$$f_D = 8\left[\left(\frac{8}{Re}\right)^{12} + \frac{1}{(A+B)^{3/2}}\right]^{1/12} \tag{A.11}$$

where,

$$A = \left[2.457 \ln\left(\frac{1}{(7/Re)^{0.9} + 0.27\varepsilon/D_h}\right)\right]^{16} \tag{A.12}$$

$$B = \left(\frac{3.753\times10^4}{Re}\right)^{16} \tag{A.13}$$

where, f_D is the Darcy friction factor, ε is the wall roughness, and D_h is the hydraulic diameter.

B. Solid Material Properties

This appendix provides the temperature-dependent solid-property functions and graphical property curves referenced in Table 8. Temperatures are in Kelvin, thermal conductivity is in W/m-K, specific heat is in J/kg-K, and density is in kg/m^3.

$$k(T)_{UC} = \begin{cases} 189.66 - 0.1176T + 1.9384\times10^{-6}T^2, & T < 1350, \\ 584.04 - 0.7502T + 2.5389\times10^{-4}T^2, & T < 1500, \\ 9.15 + 0.0328T - 1.2991\times10^{-5}T^2, & T < 1870, \\ 25, & T \geq 1870. \end{cases} \tag{B.1}$$

$$c_p(T)_{UC} = \begin{cases} \dfrac{A_0(T/1000)^N}{1 + A_1(T/1000) + A_2(T/1000)^2}\times1000, & T < 293, \\ \left(B_0 + B_1(T/1000) + B_2(T/1000)^2 + B_{-2}(T/1000)^2\right)\times1000, & T \geq 293. \end{cases} \tag{B.2}$$

$$k(T)_{graphite} = \begin{cases} 3.28248\times10^{-5}T^2 - 1.2489\times10^{-1}T + 1.69214\times10^2, & T > 500, \\ 115, & T \leq 500. \end{cases} \tag{B.3}$$

$$C_p(T)_{graphite} = 4184\left(0.54212 - 2.42667\times10^{-6}T - \frac{90.2725}{T} - \frac{43449.3}{T^2} + \frac{1.59309\times10^7}{T^3} - \frac{1.43688\times10^9}{T^4}\right) \tag{B.4}$$

$$k(T)_{SS} = -7.301\times10^{-6}T^2 + 0.02716T + 6.308 \tag{B.5}$$

$$c_p(T)_{SS} = 0.1816T + 428.46 \tag{B.6}$$

This preprint research paper has not been peer reviewed. Electronic copy available at: https://ssrn.com/abstract=7593512

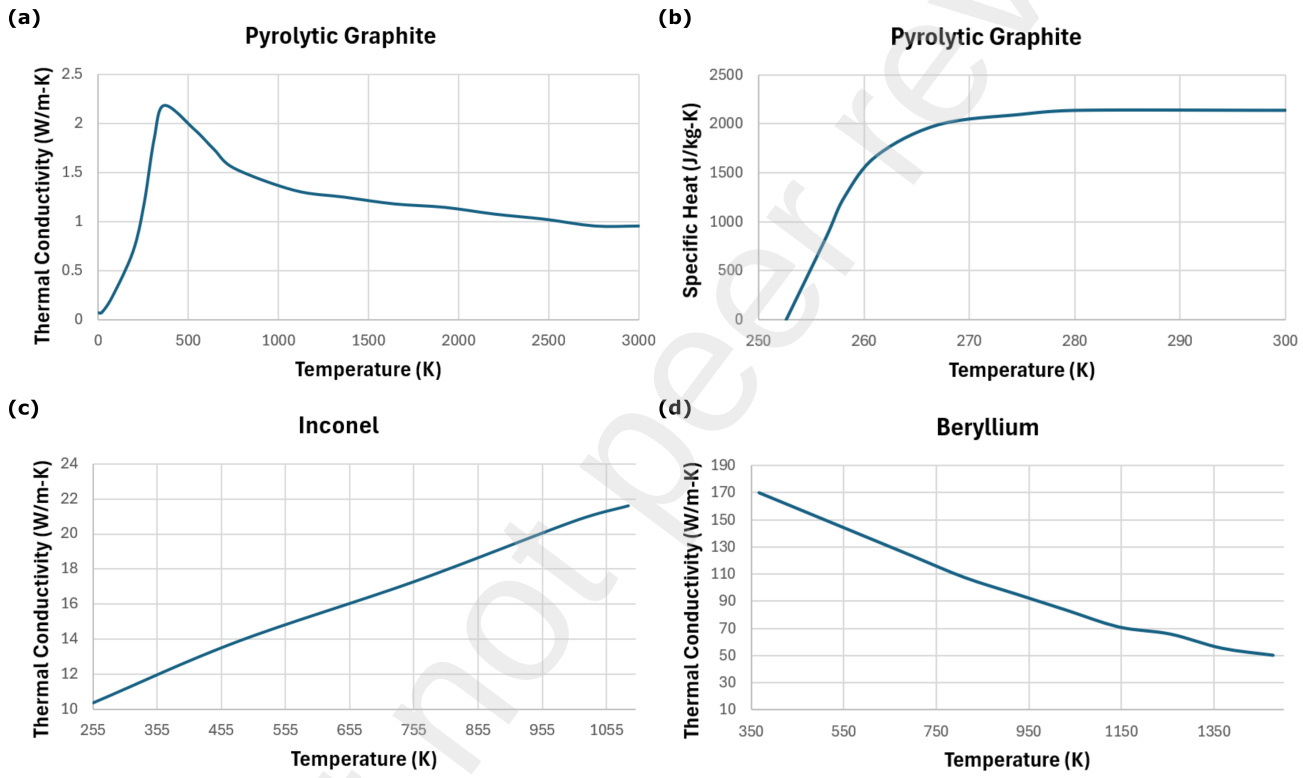

Figure 20: Material-property correlations used in the thermal-hydraulic model: (a) upper left, pyrolytic graphite thermal conductivity; (b) upper right, pyrolytic graphite specific heat; (c) lower left, Inconel thermal conductivity; and (d) lower right, beryllium thermal conductivity.

Preprint not peer reviewed

This preprint research paper has not been peer reviewed. Electronic copy available at: https://ssrn.com/abstract=7593512

CRediT authorship contribution statement

Robert Demuth: Conceptualization, Methodology, Software, Validation, Formal analysis, Investigation, Data curation, Visualization, Writing – original draft. Andrew Hanson: Software, Validation, Investigation, Writing – review and editing. Ruixian Fang: Supervision, Methodology, Writing – review and editing. Jason Reynolds: Resources, Project administration, Funding acquisition, Writing – review and editing. Travis Knight: Supervision, Conceptualization, Funding acquisition, Project administration, Writing – review and editing.

Funding

This work was supported by NASA Grant Number 80NSSC25M7034. Student support was provided through the Department of Energy Office of Nuclear Energy University Nuclear Leadership Program Graduate Fellowship and the Nuclear Regulatory Commission Graduate Fellowship Program.

Data availability

The processed benchmark data, model input files, and post-processing scripts supporting the findings will be made available upon request. Historical source data used for benchmarking are available in the cited XE-1 Nuclear Subsystem Thermal and Nuclear Design Data Book.

Declaration of competing interest

The authors declare that they have no known competing financial interests or personal relationships that could have appeared to influence the work reported in this paper.

Declaration of generative AI and AI-assisted technologies in the manuscript preparation process

During the preparation of this work, the authors used ChatGPT to assist with debugging, post-processing, grammatical review, and LaTeX editing. After using this tool, the authors reviewed and edited the generated content as appropriate and take full responsibility for the content of the published article.

Acknowledgements

This work is a collaboration between the University of South Carolina and NASA Marshall Space Flight Center.

This research made use of Idaho National Laboratory's High Performance Computing systems located at the Collaborative Computing Center and supported by the Office of Nuclear Energy of the U.S. Department of Energy and the Nuclear Science User Facilities under Contract No. DE-AC07-05ID14517, as well as the University of South Carolina Research Computing Hyperion High Performance Computing cluster, located in the University of South Carolina data center and supported by the Division of Information Technology Research Computing program.

The authors thank Jonathan Witter (BWX Technologies, Inc.) for providing an extensive collection of historical Rover/NERVA documentation and reports that supported this work. The authors also thank Andrew Ghossein (Lockheed Martin) for providing additional XE-Prime documentation and historical references.

The authors acknowledge the contribution of the 2025 Cosmic intern team at Idaho National Laboratory (Jonathan Geymer, Leo Tunkle, Wafaa Osman, and Felicity Griffin) for providing example inputs for automated OpenMC cross-section tabulation workflows used in the development of the Python scripting tools utilized in this work.

The authors additionally acknowledge Jackson Harter (Idaho National Laboratory) for his continued guidance, technical mentorship, and expertise in MOOSE-based NTP modeling and autonomous reactor control methodologies, which contributed significantly to the development of this work.

References

[1] R. Demuth, A. Hanson, R. Fang, J. Reynolds, T. Knight, A Historically Validated Thermal-Hydraulic MOOSE Model of the XE-Prime Nuclear Thermal Rocket Engine: Part II – EP-5C Experimental Validation, manuscript submitted to Progress in Nuclear Energy (2026).

[2] SKY LIGHTS, Nuclear Thermal Propulsion, [Online; accessed 2026-09-08] (2 2025).
URL https://sky-lights.org/2025/02/24/nuclear-thermal-propulsion/

[3] M. D. DeHart, S. Schunert, V. M. Labouré, Nuclear Thermal Propulsion, IntechOpen, 2022, [Online; accessed 2026-04-29]. doi:10.5772/intechopen.103895.
URL https://www.intechopen.com/chapters/81555

[4] J. L. Finseth, Rover Nuclear Rocket Engine Program: Overview of Rover Engine Tests, final Report, Tech. Rep. NASA-CR-184270, Sverdrup Technology, Inc., MSFC Group (2 1991).
URL https://ntrs.nasa.gov/citations/19920005899

[5] D. R. Koenig, Experience Gained from the Space Nuclear Rocket Program (Rover), Tech. Rep. LA-10062-H, Los Alamos National Laboratory (5 1986).

[6] W. H. Robbins, H. B. Finger, An historical perspective of the NERVA nuclear rocket engine technology program, in: AIAA/NASA/OAI Conference on Advanced SEI Technologies, American Institute of Aeronautics and Astronautics, Cleveland, OH, USA, 1991. doi:10.2514/6.1991-3451.
URL https://ntrs.nasa.gov/citations/19910017902

[7] Westinghouse Astronuclear Laboratory, Xe-1 Nuclear Subsystem Thermal and Nuclear Design Data Book, Tech. Rep. WANL-TME-1565, Westinghouse Astronuclear Laboratory (apr 15 1967).

[8] C. Eck, D. Kotlyar, Reproducible benchmark for the XE Prime experimental reactor, part i: At dry conditions, Annals of Nuclear Energy 236 (2026) 112373. doi:10.1016/j.anucene.2026.112373.

[9] J. Thomsen, C. Eck, D. Kotlyar, Application and validation of a higher-fidelity architecture for coupled neutronic and thermal-hydraulic analysis in the XE-Prime nuclear thermal propulsion system, Frontiers in Nuclear Engineering 5 (2026) 1884654. doi:10.3389/fnuen.2026.1884654.

[10] E. A. Harvego, T. K. Sulmeisters, A Comparison of Propulsion Systems for Potential Space Mission Applications, in: Space Nuclear Power Systems Symposium, Idaho National Engineering Laboratory, 1987.

Preprint not peer reviewed

This preprint research paper has not been peer reviewed. Electronic copy available at: https://ssrn.com/abstract=7593512

[11] J. Hansel, D. Andrs, L. Charlot, G. Giudicelli, The MOOSE Thermal Hydraulics Module, Journal of Open Source Software 9 (94) (2024) 6146. doi:10.21105/joss.06146.

[12] Z. Qi, W. Han, M. Liu, C. Ji, H. Wei, S. Huang, Ntpss-vPower: A model for system simulation of a nuclear thermal propulsion system, Annals of Nuclear Energy 192 (2023) 110019. doi:10.1016/j.anucene.2023.110019.

[13] V. Gnielinski, Heat Transfer Coefficients for Turbulent Flow in Concentric Annular Ducts, Heat Transfer Engineering 30 (6) (2009) 431–436. doi:10.1080/01457630802528661.

[14] Aerojet Nuclear Systems Company, Materials Properties Data Book, Tech. Rep. Report 2275, Aerojet Nuclear Systems Company, Sacramento, California (8 1970).

[15] Aerojet Nuclear Systems Company, Materials Properties Data Book: Volume 3, Nonmetallics and Appendices, Tech. Rep. Report 2275, Aerojet Nuclear Systems Company, Sacramento, California (8 1970).

[16] R. D. McCarty, J. Hord, H. M. Roder, Selected properties of hydrogen (engineering design data), Tech. Rep. NBS MONO 168, National Bureau of Standards, Gaithersburg, MD (1981). doi:10.6028/NBS.MONO.168.
URL https://nvlpubs.nist.gov/nistpubs/Legacy/MONO/nbsmonograph168.pdf

[17] G. Giudicelli, C. Green, J. Hansel, D. Andrs, A. Novak, S. Schunert, B. Spaude, S. Isaacs, M. Kunick, R. Salko, S. Henderson, L. Charlot, A. Lindsay, The MOOSE fluid properties module, Computer Physics Communications 307 (2025) 109407. doi:10.1016/j.cpc.2024.109407.

[18] Y. Fang, C. Wang, W. Tian, D. Zhang, G. Su, S. Qiu, Study on high-temperature hydrogen dissociation for nuclear thermal propulsion reactor, Nuclear Engineering and Design 392 (2022) 111753. doi:10.1016/j.nucengdes.2022.111753.

[19] J. P. McDonald, C. D. Smith, A. D. Boylston, Parahydrogen Thermophysical Properties V05 Final Report, Tech. Rep. SNP-DOC-0046, National Aeronautics and Space Administration, George C. Marshall Space Flight Center, Marshall Space Flight Center, Alabama (jul 1 2024).

[20] C. Smith, J. Stonehill, Impact of Real Gas Properties on Multiphysics Modeling of a Nuclear Thermal Propulsion Fuel Element, in: Transactions of the American Nuclear Society, Vol. 132, Chicago, IL, USA, 2025, pp. 44–47.
URL https://ntrs.nasa.gov/citations/20250002665

Preprint not peer reviewed

This preprint research paper has not been peer reviewed. Electronic copy available at: https://ssrn.com/abstract=7593512